Underwater UXO Detection and Discrimination: Understanding EMI Scattering Phenomena in a Conducting Environment

Fridon Shubitidze[a,b], Benjamin Barrowes[c], Irma Shamatava[a,b], Juan Pablo Fernández[a], and Kevin O'Neill[a,c]

[a] Thayer School of Engineering, Dartmouth College, Hanover NH, 03755 , USA;
[b] Sky Research, Inc. Hanover, NH, 03755;
[c] USA ERDC Cold Regions Research and Engineering Laboratory,
72 Lyme Road, Hanover NH, 03755, USA

Email: Fridon.Shubitidze@dartmouth.edu

ABSTRACT

There are approximately one million acres of underwater lands at Department of Defense (DOD) and Department of Energy (DOE) sites that are highly contaminated with unexploded ordnance (UXO) and land mines. The detection and disposal of Underwater Military Munitions are more expensive than excavating the same targets on land. Electromagnetic induction (EMI) sensing has emerged as one of the most promising technologies for underwater detection. In order to explore the full potential of various EMI sensing technologies for underwater detection and discrimination, to achieve a high (~100%) probability of detection, and to distinguish UXO from non-UXO items accurately and reliably, first the underlying physics of EM scattering phenomena in underwater environments needs to be investigated in great detail. This can be achieved by using an accurate 3D numerical code, such as the combined method of auxiliary sources and thin skin depth approximation (MAS/TSA), the pseudospectral time-domain technique, finite element methods or other approaches. This paper utilizes the combined MAS/TSA, originally developed for detection and discrimination of highly conducting and permeable metallic objects placed in an environment with zero or negligible conductivity. Here, first the theoretical basis of the MAS/TSA is presented for metallic objects placed in an electrically conductive environment. Then numerical experiments are conducted for homogeneous targets of canonical (spheroidal) shapes subject to frequency- or time-domain illumination. The results illustrate coupling effects between the object and its surrounding conductive medium, particularly at high frequencies (early times for time-domain sensors), and the way this coupling depends on the distance between the sensor and the object's center.

Keywords: UXO, detection/discrimination, MAS model, skin depth, modeling, underwater, conducting environments

1. INTRODUCTION

Modern electromagnetic induction (EMI) digital geophysical technologies such as magnetic and time- and frequency-domain sensors [1]–[5] have been used effectively to characterize potentially harmful subsurface munitions on dry land [6]–[20]. However, by estimation there may be as many as one million acres of formerly used military underwater land contaminated with hazardous UXO [22]–[23]. Underwater environments, unlike dry soil, are electrically conducting and heterogeneous. This significantly affects the performance of established and emerging land-based EMI sensing technologies [24]–[25], since the electrical conductivity of water is much higher than the conductivity of soil. An object's underwater EM response should be less than its response in dry soil because water absorbs EM energy much faster than dry soil, particularly at high frequencies where skin effects are significant. In this paper the generalized MAS/TSA technique is employed to illustrate these physical phenomena and to understand low-frequency electromagnetic scattering phenomena from highly conducting and permeable metallic objects embedded in marine environments.

The Method of Auxiliary Sources (MAS) is a numerical technique originally designed for solving various electromagnetic radiation and scattering problems. The MAS is a robust, easy to implement, and accurate method for studying a wide range of electromagnetic problems, such as the investigation of waveguide structures, antennas,

Detection and Sensing of Mines, Explosive Objects, and Obscured Targets XIII,
edited by Russell S. Harmon, John H. Holloway, Jr., J. Thomas Broach,
Proc. of SPIE Vol. 6953, 69530M, (2008) · 0277-786X/08/$18 · doi: 10.1117/12.777876

scattering, electromagnetic wave propagation in complex media, etc. The MAS has also been used successfully in the analysis of low-frequency electromagnetic induction scattering phenomena [26]–[29]. EMI boundary-value problems [26] are solved numerically by representing the electromagnetic fields in each domain of the structure under investigation by a finite linear combination of analytical solutions of the relevant field equations, corresponding to sources situated some distance away from the boundaries of each domain. These "auxiliary sources" producing the analytic solutions are chosen to be elementary currents/charges located on fictitious auxiliary surfaces usually conforming to the actual surfaces of the structure. The method only requires points on the auxiliary and actual surfaces, without resorting to the detailed mesh structures required by other techniques such as finite element methods (FEM), boundary element methods (BEM), etc.

The two auxiliary surfaces are set up inside and outside the penetrable scattering object. Specifically, the fields outside of the structure are considered to originate from a set of auxiliary sources placed inside the object, while the fields penetrating inside the object arise from a set of auxiliary sources placed outside the object. The fields constructed inside and outside of the object are required to obey the continuity of the tangential magnetic field component and the jump condition for the normal magnetic field component at an array of selected points on the physical surfaces of the structure. The results are matrix equations in which the amplitudes of the auxiliary sources are to be determined. Once the amplitudes of the auxiliary sources are found, the solution is complete; the magnetic or electromagnetic fields and related parameters can easily be computed throughout the interior and exterior domains.

Usually, EMI scattering responses are expressed relative to the induction number $\chi \equiv \sqrt{-2j\pi\nu\sigma\mu}\, a$, where j is the imaginary unit, a (m) is a characteristic (usually the smallest) dimension of the object, ν (Hz) is the frequency, $\mu = \mu_o\mu_r$ (H/m) is the magnetic permeability, and σ (S/m) is the scatterer's electrical conductivity. The quantity χ is proportional to a/δ, where δ (m) is the skin depth. It is very well established that the electromagnetic field in the interior domain decays over distances of the order of the skin depth (high induction number). This reduces the efficiency and accuracy of the MAS. To overcome this problem, a combined MAS-thin skin approximation (MAS-TSA) [28,30] has been developed and widely used for solving a variety of EMI problems from 0 Hz (magnetostatic regime) up to 1 MHz. The MAS/TSA algorithm has been tested and has shown excellent agreement with experimental data for canonical objects (cylinders, spheroids, etc.) as well as for real UXO, under non-uniform field excitations [28]. Based on the hybrid full MAS at low frequencies and the combined MAS-TSA algorithm at high frequencies, a user-friendly EMI BOR code has been developed for state-of-the-art EMI sensors in both frequency and time domains (the time-domain signal is obtained from that in the frequency domain through a Fourier transform) [27]. In this paper the MAS/TSA technique is extended to consider highly conducting and permeable metallic objects placed in a conducting and permeable medium to study how marine environments change the phenomenology of EMI sensors and how these changes can affect their ability to discriminate between UXO and non-UXO items.

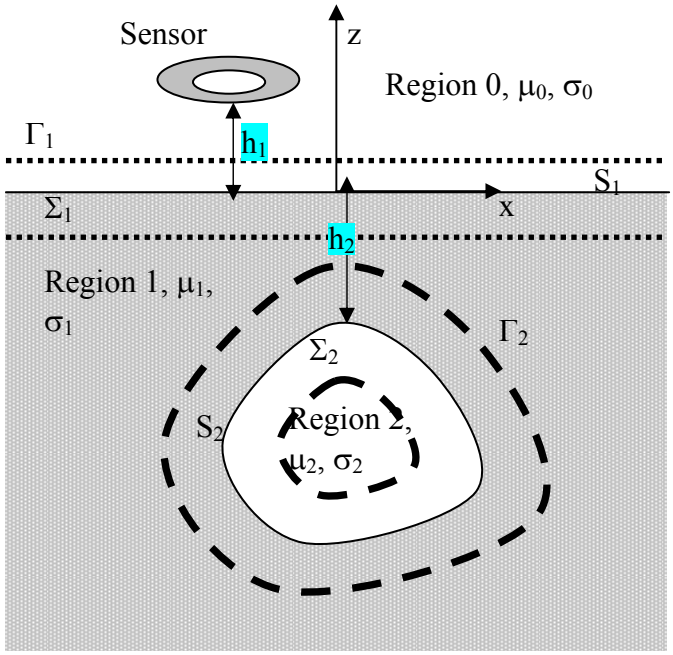

Figure 1. Problem geometry.

The paper is organized as follows: In Section 2 the MAS technique is presented for highly conducting and permeable metallic objects embedded in a uniform conductive and permeable space. Section 3 describes the thin skin depth approximation for a conductive space. In Section 4 numerical results are presented for a conductive and permeable

sphere and spheroid illuminated with current state-of-the-art sensors in both frequency and time domains; the interaction between the sensor and the surrounding medium is demonstrated. Finally, in Section 5 conclusions are given.

2. THE METHOD OF AUXILIARY SOURCES FOR UNDERWATER ENVIRONMENTS

To illustrate the MAS for an underwater object, let us consider a permeable, conducting 3-D object placed in a conducting half space. The object is illuminated with a time-varying electromagnetic field originated from the sensor (Figure 1). The computational region is divided into three parts: the $z > 0$ half-space (referred to as Region 0) with free-space electromagnetic parameters, Region 1 corresponding to the soil with ε_1, σ_1, μ_1, and Region 2 referring to the target with ε_2, σ_2, μ_2 as parameters (Figure 1). As is well established, in the EMI frequency regime the displacement currents are negligible. The primary field induces eddy currents within the conductive regions, which in turn produce secondary (scattered) fields. The magnetic field inside each region can be expressed as

$$\mathbf{H}_\alpha(\vec{\mathrm{r}}) = \mathrm{k}_\alpha^2 \boldsymbol{\Pi}_\alpha^{\mathrm{m}}(\mathbf{r}) + \nabla\nabla\cdot\boldsymbol{\Pi}_\alpha^{\mathrm{m}}(\mathbf{r}) \ , \tag{1}$$

where

$$\boldsymbol{\Pi}_\alpha^{\mathrm{m}}(\mathbf{r}) = \sum_{\mathrm{i}=1} \frac{1}{4\pi\mu_\alpha} \frac{\mathbf{P}_{\alpha,\mathrm{i}}^{\mathrm{ou}} e^{-\mathrm{j}\mathrm{k}_\alpha \left|\mathbf{r}-\mathbf{r}_{\alpha,\mathrm{i}}^{\mathrm{ou}}\right|}}{\left|\mathbf{r}-\mathbf{r}_{\alpha,\mathrm{i}}^{\mathrm{ou}}\right|} + \sum_{\mathrm{i}=1} \frac{1}{4\pi\mu_\alpha} \frac{\mathbf{P}_{\alpha+1,\mathrm{i}}^{\mathrm{in}} e^{-\mathrm{j}\mathrm{k}_\alpha \left|\mathbf{r}-\mathbf{r}_{\alpha+1,\mathrm{i}}^{\mathrm{i}}\right|}}{\left|\mathbf{r}-\mathbf{r}_{\alpha+1,\mathrm{i}}^{\mathrm{in}}\right|} . \tag{2}$$

Here $\boldsymbol{\Pi}_\alpha^{\mathrm{m}}(\mathbf{r})$ is the fundamental solution of the Helmholtz equation, $\mathrm{k}_\alpha = \sqrt{-\mathrm{j}\omega\sigma_\alpha\mu_\alpha}$, $\alpha = 0,1,2$, $\mathbf{P}_{\alpha,\mathrm{i}}^{\mathrm{ou}}$ and $\mathbf{P}_{\alpha+1,\mathrm{i}}^{\mathrm{in}}$ are the i^{th} unknown magnetic dipole source coefficients distributed on the outer auxiliary surfaces Γ_α and Σ_α at points $\mathbf{r}_{\alpha+1,\mathrm{i}}^{\mathrm{ou}}$ and $\mathbf{r}_{\alpha+1,\mathrm{i}}^{\mathrm{in}}$ respectively. A time dependence $e^{j\omega t}$ is assumed and suppressed in all subsequent discussions. The vector $\mathbf{P}_{\alpha,\mathrm{i}}^{\mathrm{ou}}$ consists of two components approximately parallel to the real surface (or, equivalently, two crossed magnetic-current elements), and $\mathbf{P}_{\alpha,\mathrm{i}}^{\mathrm{in}} = \mathrm{P}_{\alpha,\mathrm{i}}^{\mathrm{in}}\ \hat{\mathbf{n}}_{\mathrm{i}}$ has only one component normal to the real surface. We compute the total field inside each region α ($\alpha = 0,1,2$) by assuming that these sources radiate into an infinite homogeneous medium with the properties of the corresponding region.

The electromagnetic fields at each interface between two regions are connected by boundary conditions. Specifically, the tangential component of the magnetic field and the normal component of the magnetic flux density must be continuous across real surface:

$$\begin{aligned} [\hat{\mathbf{n}}\times(\mathbf{H}_\alpha^{\mathrm{tot}} - \mathbf{H}_{\alpha+1}^{\mathrm{tot}})] &= \mathbf{0} \\ \hat{\mathbf{n}}\cdot(\mathbf{B}_\alpha^{\mathrm{tot}} - \mathbf{B}_{\alpha+1}^{\mathrm{tot}}) &= 0 \end{aligned} \tag{3}$$

where $\hat{\mathbf{n}}$ is a unit normal vector on the interface between the two regions. In the numerical implementation we consider the surface of the body to be smooth. The real (physical) surface S_α is divided into M subsurfaces. For each m^{th} subsurface, at a location point $\mathbf{r}_m$ the surface normal unit vector $\hat{\mathbf{n}}_{\mathrm{m}}$ and surface tangential vectors $\hat{\mathbf{s}}_{\mathrm{m}}$ and $\hat{\mathbf{t}}_{\mathrm{m}}$ are determined, with $\hat{\mathbf{n}}_{\mathrm{m}} = [\hat{\mathbf{t}}_{\mathrm{m}} \times \hat{\mathbf{s}}_{\mathrm{m}}]$. Similarly, the auxiliary surfaces are divided into a finite number N of subsurfaces. Continuity of tangential components of magnetic field and normal components of magnetic flux density vector is enforced at $m = 1, 2, \ldots, M$ points over the physical boundary S_α. Assuming that $\mathrm{M} \geq \mathrm{N}$, this provides a sufficient number of independent linear equations to determine the unknown coefficients $\left\{\mathbf{P}_{\alpha,\mathrm{i}}^{\mathrm{ou}}\right\}$ and $\left\{\mathbf{P}_{\alpha,\mathrm{i}}^{\mathrm{in}}\right\}$. Once the unknown

coefficients of the auxiliary sources are obtained, the approximate field can be evaluated easily in either region by simple summation of the source influences.

3. THE TSA FOR UNDERWATER ENVIRONMENTS

Studies show that at high frequencies, where the skin depth becomes much smaller than the characteristic lengths of the scatterers, the accuracy and computational efficiency of the MAS degrades; this is the case for other methods as well [12]. To avoid these difficulties, a combined MAS/TSA algorithm has been developed for metallic objects placed in free space. Here the MAS/TSA approach is extended to include objects embedded in a conducting medium. The essential difference here is that scattered field outside the object is approximated as sum of magnetic fields produced by elementary magnetic dipoles. These dipole sources are assumed to radiate in an unbounded homogenous space with the material properties of the medium surrounding the object. The details of the MAS/TSA formulation for objects in free space are given in references [27]–[29] and are only summarized here.

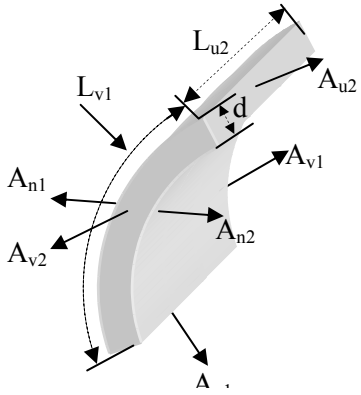

Figure 2. Geometry of a volume just below the real surface S.

As in reference [28], the formulation proceeds by constructing a thin volume just below a patch of the scatterer's surface (Fig 2). The approximation assumes that the normal component of the magnetic field varies approximately one-dimensionally normal to the surface. In particular, the TSA assumes that, just below the surface, the relation between the normal magnetic field component and its normal derivative is the same as in the solution to the 1-D Helmholtz equation: $\partial H_n / \partial n \approx -jkH_n$. Maxwell's divergence equation for magnetic fields also applies in the small volume. After integrating it and taking the limit when the thickness d of the volume approaches zero, we can use the boundary conditions to express the necessary internal variables entirely in terms of quantities pertaining to the external fields, somewhat in the manner of an impedance boundary condition. That is, for the region corresponding to the surface patch A_n in Figure 2 we have

$$[Z][Q] = -[Y], \tag{4}$$

where

$$[\mathrm{Z}] = \left[\mathrm{G}_{\mathrm{n}}^{\mathrm{P^{in}}} \ \frac{1}{\mu_{\ell,\mathrm{r}}} \left(jk_{\ell}\mathrm{A}_{\mathrm{n}} + \frac{\partial \mathrm{A}_{\mathrm{n}}}{\partial \mathrm{n}} \right) \right] + \left[\mathrm{G}_{\mathrm{u}_2}^{\mathrm{P^{in}}} \mathrm{L}_{\mathrm{u}_2} - \mathrm{G}_{\mathrm{u}_1}^{\mathrm{P^{in}}} \mathrm{L}_{\mathrm{u}_1} + \mathrm{G}_{\mathrm{v}_2}^{\mathrm{P^{in}}} \mathrm{L}_{\mathrm{v}_2} - \mathrm{G}_{\mathrm{v}_1}^{\mathrm{P^{in}}} \mathrm{L}_{\mathrm{v}_1} \right] \tag{5}$$

and

$$[\mathrm{Y}] = \left[\mathrm{H}_{\mathrm{n}}^{\mathrm{pr}} \frac{1}{\mu_{\ell,\mathrm{r}}} \left(jk_{\ell}\mathrm{A}_{\mathrm{n}} + \frac{\partial \mathrm{A}_{\mathrm{n}}}{\partial \mathrm{n}} \right) \right] + \left[\mathrm{H}_{\mathrm{u}_2}^{\mathrm{pr}} \cdot \mathrm{L}_{\mathrm{u}_2} - \mathrm{H}_{\mathrm{u}_1}^{\mathrm{pr}} \cdot \mathrm{L}_{\mathrm{u}_1} + \mathrm{H}_{\mathrm{v}_2}^{\mathrm{pr}} \cdot \mathrm{L}_{\mathrm{v}_2} - \mathrm{H}_{\mathrm{v}_1}^{\mathrm{pr}} \cdot \mathrm{L}_{\mathrm{v}_1} \right] \tag{6}$$

with

$$\mathrm{G}_{\alpha}^{\mathrm{p^{in}}} = \left(\bar{\bar{\mathbf{G}}}(\mathbf{r}_{\mathrm{m}}, \mathbf{r}_{\mathrm{i}}) \cdot \hat{\mathbf{n}}_{\mathrm{i}} \right) \cdot \hat{\boldsymbol{\alpha}}_{\mathrm{m}} . \tag{7}$$

Here H_{α}^{pr} is the primary magnetic field along the $\alpha = \mathrm{n}, \mathrm{u}_1; \mathrm{u}_2; \mathrm{v}_1$ and v_2 directions, A_{n} is the area of the patch, $\mathrm{L}_{\alpha,\mathrm{i}}$ is its length along the $\alpha = \mathrm{n}, \mathrm{u}_1; \mathrm{u}_2; \mathrm{v}_1$ and v_2 directions, $\hat{\boldsymbol{\alpha}}_{\mathrm{m}}$ is a unit vector along $\mathrm{i}\,\alpha = \mathrm{n}, \mathrm{u}_1; \mathrm{u}_2; \mathrm{v}_1$ and v_2 directions,

$\overline{\overline{\mathbf{G}}}(\mathbf{r}_m, \mathbf{r}_i) \cdot \hat{\mathbf{n}}_i$ is the magnetic field at $\mathbf{r}_m$ produced by a unit dipole placed at $\mathbf{r}_i$ and oriented along $\hat{\mathbf{n}}_i$, and $\overline{\overline{\mathbf{G}}}(\mathbf{r}_m, \mathbf{r}_i)$ is the dyadic Green's function for a unit magnetic dipole. A more explicit form of the matrix $\overline{\overline{\mathbf{G}}}(\mathbf{r}_m, \mathbf{r}_i)$ is given in [26]. All the electromagnetic quantities in (4)–(6) pertain to the exterior field; no explicit solution for the internal field is required; and the mesh resolution needed is only that required for defining the geometry adequately. This overall approach has proved both accurate and extremely efficient for both frequency- and time-domain electromagnetic induction problems.

4. RESULTS

In this section numerical experiments are designed to demonstrate the interaction effects between a highly conducting and permeable metallic object and its surrounding conducting medium. First the accuracy of the MAS/TSA technique is checked for a sphere placed in the medium. A comparison between MAS/TSA and analytic data is shown in Figure 3 for a non-permeable sphere of radius $a = 5$ cm and conductivity $\sigma = 10^7$ S/m placed in a uniform space of conductivity 4 S/m and illuminated by a uniform time-varying primary magnetic field directed along the z-axis. Comparisons are given for two observation points (10 cm and 15 cm above the center of the sphere). The magnetic fields are normalized so their quadrature parts peak at unity. These results show that the numerical (MAS/TSA) and analytical results are in excellent agreement, demonstrating the validity of both approaches for metallic objects placed in a conducting space. Figure 3 shows that the strong interaction between the sphere and its surrounding space occurs mostly at high frequencies. Both the inphase and the quadrature parts change as a result of the interaction: the inphase part turns toward zero and the quadrature part changes sign at high frequency as the response from the water becomes dominant. Results also show that the interaction depends on the observation point. For instance, Figure 3 shows that, as the observation distance from the sphere increases, the interaction between the object and the host medium shifts toward lower frequencies.

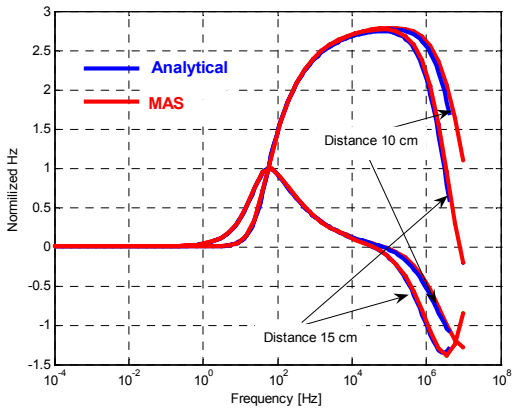

Figure 3. Normalized scattered magnetic field versus frequency for a sphere.

Next, to illustrate the applicability of the MAS /TSA for modeling state-of-the-art EMI sensors placed in underwater environments we study the interaction between the Geophex GEM-3 frequency-domain sensor (www.geophex.com) and a surrounding conductive host medium. The GEM-3 sensor consists of two concentric transmitter loops (see cross section in Figure 4 [2]). The currents in these loops circulate in opposite directions and are scaled so that the total primary field vanishes at the common center, where a receiving coil is located. The transmitter loops are idealized as infinitely thin line sources of radii a_1 and a_2 with currents $I_2 = -I_1 a_2/a_1$. It is obvious that in underwater environments the sensor electronics need to be protected from the water; this can be achieved by putting the sensor in a box (Figure 4). For this demonstration we take a box of diameter 60 cm and height 5 cm; the surrounding medium has conductivity $\sigma = 1$, 4 and 10 S/m, and permeability $\mu_r = 1$.

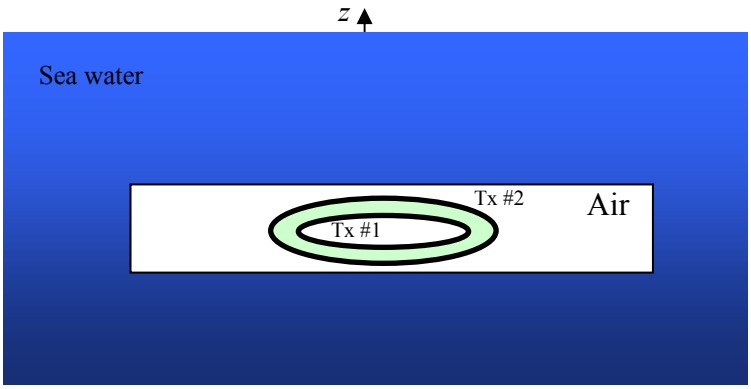

Figure 4. Schematic diagram on the x-z plane ($y = 0$) of the GEM-3 sensor placed under water.

=The secondary magnetic fields as a function of frequency for the three different conductivities are shown in Figure 5 (left: inphase part; right: quadrature part). The results show that as the conductivity of the water increases the response of the surrounding medium shifts towards lower frequencies, as expected. In addition, for conducting sea water with $\sigma = 1$ S/m the frequency response of the host medium is negligible within the GEM-3 frequency range (30 Hz up to 50 kHz); however, for higher conductivities (4 and 10 S/m, which are realistic values for sea water) the responses can be significant. This means that the surrounding medium produces additional noise that will decrease the signal-to-noise ratio and will complicate discrimination. Therefore, to improve the detection of underwater metallic objects and to better discriminate UXO from non-UXO items in marine environments we have to take into account the interaction between the sensor and its surrounding medium. One way to analyze the physics of EMI scattering phenomena in great detail for underwater environments is to investigate near-field distributions. Note that the MAS technique has the potential for simulating near as well as far fields. As a demonstration, here the near-field distributions were simulated for the GEM-3 sensor (Figure 4) surrounded by a conducting medium with $\sigma = 4$ S/m. Figure 6 shows the near-field distribution for three different frequencies, 1 kHz, 30kHz, and 50 kHz; the left column corresponds to the conducting medium and the right column to free space. The near-field distributions clearly show that at the low frequency (1 kHz) the magnetic field distribution is identical in free space and in the conducting medium. However, at high frequencies (30 kHz and 50 kHz), the magnetic field in the conducting medium is smaller than that in free space when the sensor is at the same distance. As the frequency increases, these differences become more significant. Thus the near-field distribution shows that in conductive media the EMI field decays in two ways: it decays as a function of distance just like in free space, and it decays exponentially because the EMI field is being absorbed in a conductive medium where the induction number is purely imaginary. This illustrates one more time that, in order to discriminate between UXO and non-UXO items in underwater environments, the exponential decay characteristics needs to be taken into account.

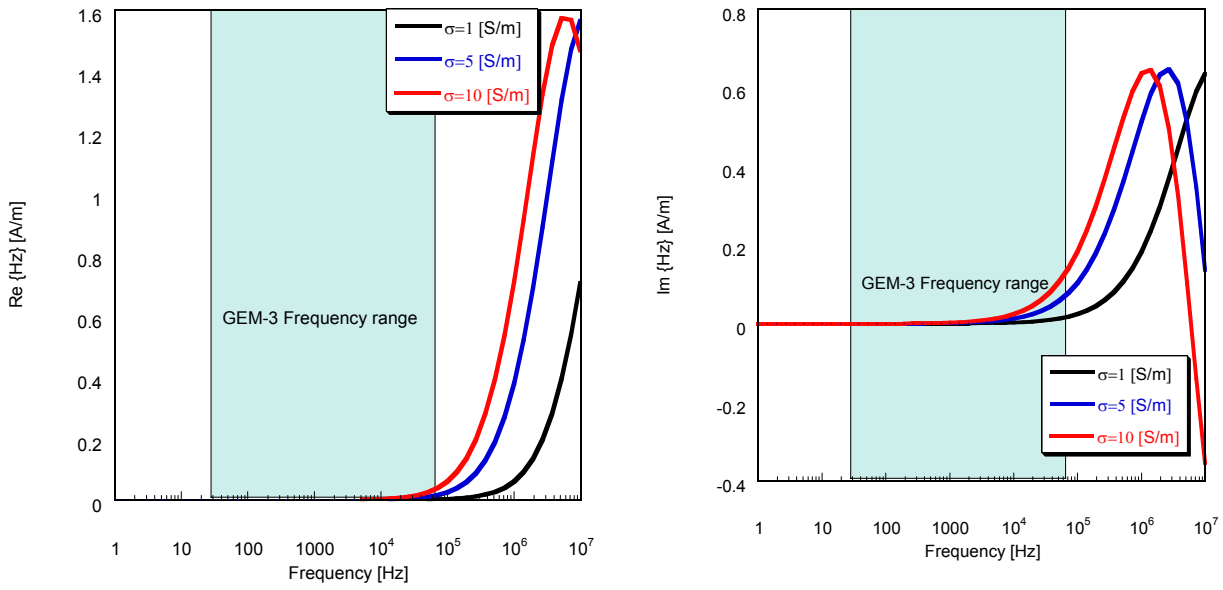

Figure 5. Scattered magnetic field versus frequency: inphase part on the left and quadrature part on the right

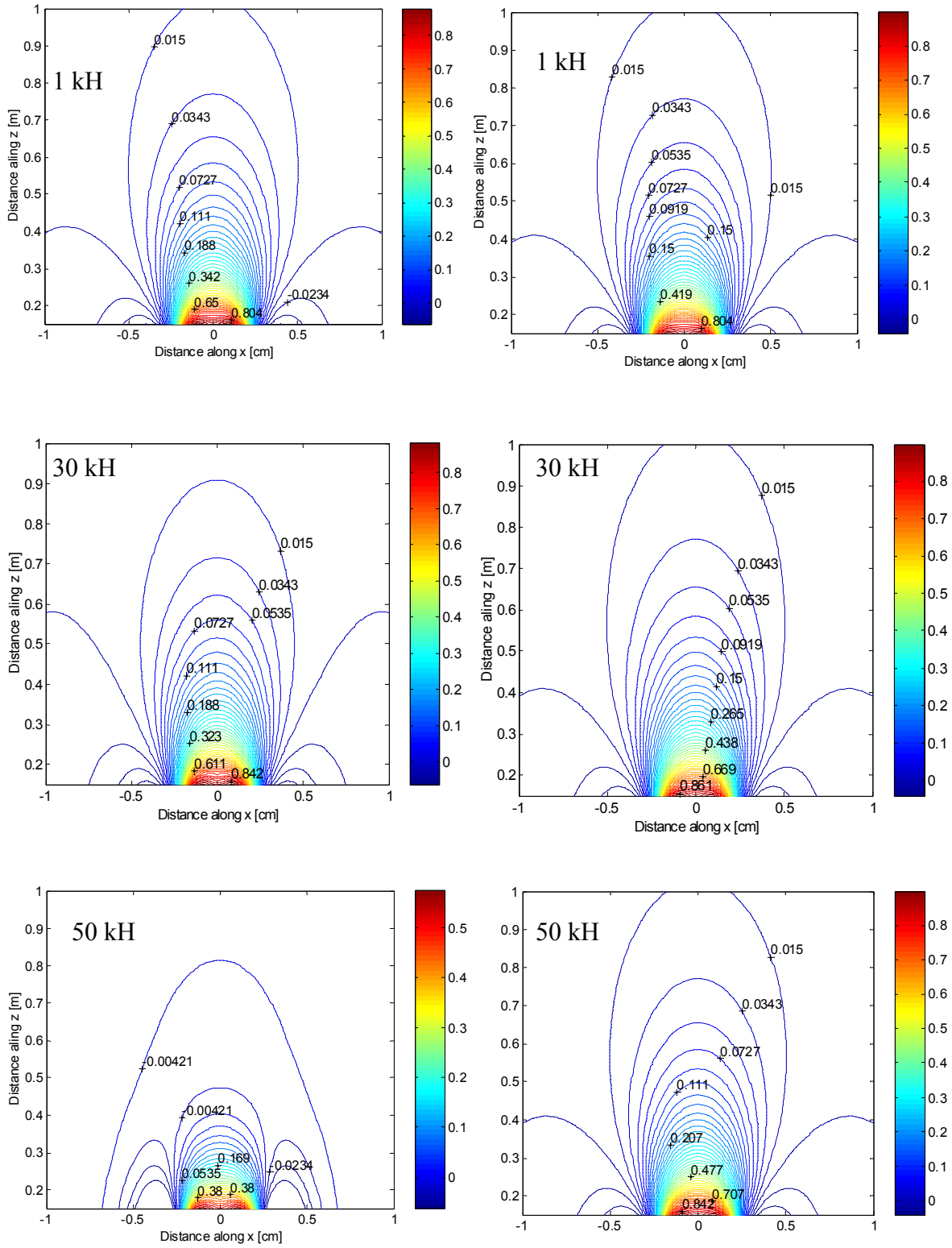

Figure 6. Near-field distribution for the GEM-3 sensor under water.

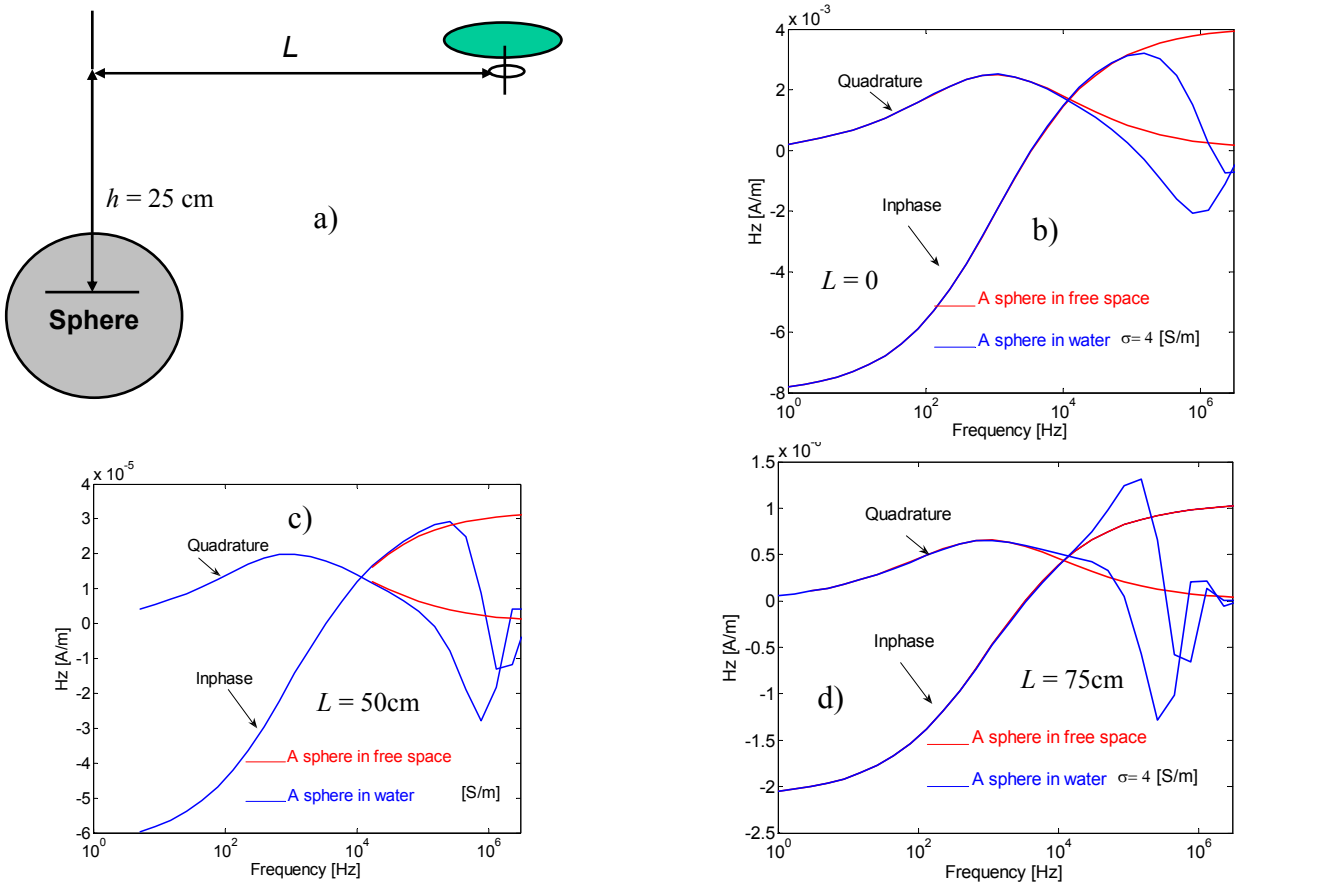

Figure 7. EMI response of a sphere illuminated by a GEM-3 sensor placed at different locations: L = 0, 50 and 75 cm.

As a next example, the MAS/TSA is applied to a highly conducting and permeable sphere, placed in a conductive medium and illuminated with the GEM-3 sensor, to illustrate how an underwater object's EMI responses depend on the distance between sensor and object. Figure 7 shows the EMI response for a sphere of radius a = 5 cm, conductivity 5×10^6 S/m, and relative permeability 100 placed 1) in a uniform medium with σ = 4 S/m conductive and 2) in non-conductive/free space. The sensor is placed at three different locations: L = 0, 50, and 75 cm. The figure clearly demonstrates the existence of significant interactions between the object and the surrounding conductive medium, particularly at high frequency. In addition, the results show that this interaction depends on the distance between the object's center and the sensor. In particular, we see that when the sensor is just above the object both inphase and quadrature parts decrease after 10 kHz; on the other hand, for L=50 cm and L=75 cm both parts first increase and then start to decrease again. These phenomena have been observed experimentally [24]. Similar tests were done for an elongated metallic object, a prolate spheroid with major and minor axes b and a, aspect ratio b/a=3, and a=5cm.

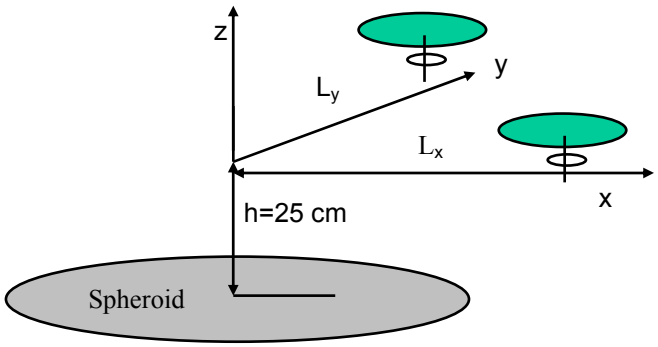

Figure 8. A spheroid in the GEM-3 field.

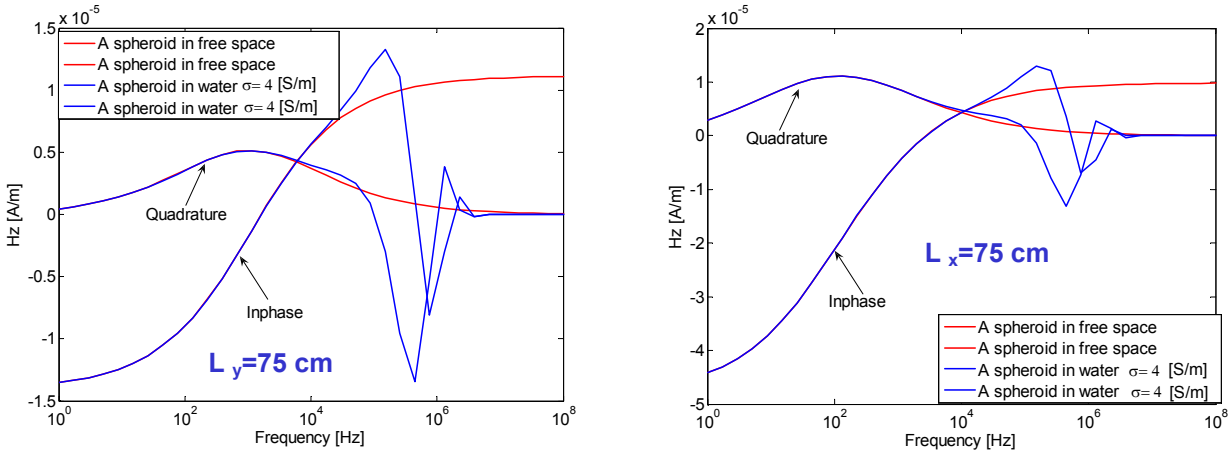

Figure 9. EMI response for a prolate spheroid with conductivity 4×10^6 S/m and permeability 100 illuminated with the GEM-3 sensor placed at location $L_x = L_y = 75$ cm.

The results are depicted in Figure 9. In this simulation the spheroid was oriented horizontally. Overall, the results for the spheroid are similar to those for the sphere; however, the interaction effect when the spheroid is under the GEM-3 with $L_y = 75$ cm is much more significant, compared to the free-space EMI response, than that for the case with $L_x = 75$ cm. This result illustrates that there is an orientation effect as well.

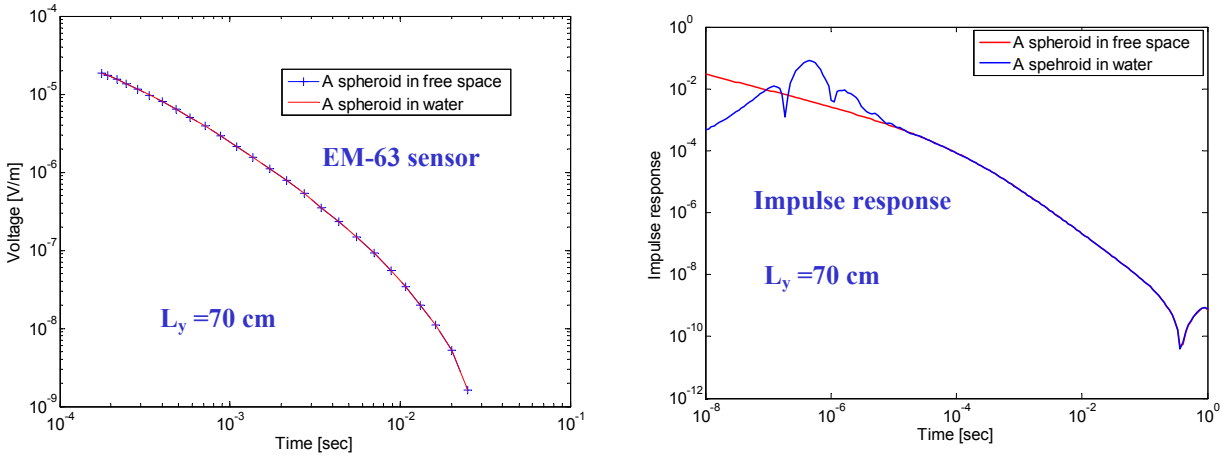

Figure 10. Time-domain EMI response of a prolate spheroid with conductivity 4×10^6 [S/m] and permeability 100, illuminated with the EM-63 time-domain sensor placed at location $L_y = 75$ cm.

Finally, time-domain EM scattering is investigated for the spheroid subject to excitation by the Geonics time-domain EM-63 sensor [3]. The sensor consists of a 1 m × 1 m square transmitter loop and two receiver loops: (1) a main receiver loop 0.5 m × 0.5 m in size whose center coincides with the transmitter coil's center, and (2) a receiver loop of the same size located 60 cm above the main receiver coil. These receivers accurately measure the complete transient response over a wide dynamic range of time from 180 μs to 25 ms. The time-domain data are calculated for the horizontal spheroid at a depth 25 cm below the sensor. The senor's center is offset 75 cm from the spheroid's center. The

EMI responses are calculated for the spheroid placed in free space and in a uniform conductive medium. Figure 10 compares the two EMI responses over the time range from 180μs to 25ms, and the impulse response over a wider time range. The figure shows that, for the spheroid placed in free and conductive space, time domain EMI responses in the time range of 180μs to 25ms are virtually the same, whereas the impulse responses calculated over a wider time frame exhibit substantial differences, particularly at early times.

5. CONCLUSION

In this paper, the combined MAS/TSA algorithm is extended for highly conducting and permeable metallic objects placed in a conducting medium with properties similar to those of an underwater environment. The accuracy of the technique is tested against the analytical solution for a conducting sphere excited by a uniform magnetic field. The numerical results demonstrate the strong coupling effects between the metallic objects and the surrounding conductive space, particularly at high frequencies (or very yearly times); these coupling effects are found to depend on the distance between the object and the sensor. Numerical analyses were done for both frequency- and time-domain sensors.

Acknowledgment. This work was supported by the Strategic Environmental Research and Development Program, Projects MM-1572 and MM-1437.

REFERENCES

1. E. Gasperikova, "Berkeley UXO discriminator (BUD) for UXO detection and discrimination," SERDP and ESTCP's Partners in Environmental Technology Technical Symposium & Workshop, Washington, DC, Nov. 28–30, 2006.
2. I.J. Won; D.A. Keiswetter; T.H. Bell, "Electromagnetic induction spectroscopy for clearing landmines," IEEE Trans. Geoscience and Remote Sensing, Vol. 39. No. 4., pp. 703–709, April 2001.
3. McNeill, J. d., and Bosnar, M., 1996. Application of Time Domain Electromagnetic Techniques to UXO Detection. Proceedings of UXO Forum '96.
4. D.M. Cargile, D.M., Bennett, H. H., Goodson, R. A., DeMoss, T. A., and Cespedes, E. R., 2004. Advanced uxo detection/discrimination technology demonstration, kahoolawe, hawaii. Technical Report ERDC/EL TR-04-1, U.S. Army Engineer Research and Development Center. Department of Defense, 2003. Estcp cost and performance report (ux-0035): Geonics em63 multichannel EM data processing algorithms for target location and ordnance discrimination. Technical Report UX-0035, Environmental Security Technology Certification Program.
5. Barrowes, Benjamin "Handheld Frequency Domain Vector EMI Sensing for UXO Discrimination" SERDP MM1537 - FY06 Annual Report, The Strategic Environmental Research and Development Program (SERDP) 2006.
6. L. R. Pasion and D. W. Oldenburg, "A discrimination algorithm for UXO using time domain electromagnetics", *Journal of Engineering and Environmental Geophysics*, vol. 28, no. 2, pp. 91-102, 2001.
7. S.V. Chilaka, D.L. Faircloth, L.S. Riggs, H. H. Nelson, H.H.; "Enhanced discrimination among UXO-like targets using extremely low-frequency magnetic fields" *IEEE Trans. Geosci. Remote Sens.,* vol. 44, no. 1, pp. 10–21, Jan. 2006.
8. S. Billings, "Practical Discrimination Strategies for Application to Live sites", *SERDP and ESTCP's Partners in Environmental Technology Technical Symposium & Workshop* Washington, D.C. November 28-30, 2006.
9. N. Geng, K.E. Baum, L. Carin, "On the low frequency natural responses of conducting and permeable target," *IEEE Trans. Geoscience and Remote Sensing*, vol. 37, pp. 347–359, 1999.
10. P. Gao, L. Collins, P. Garber, N. Geng, and L. Carin, "Classification of landmine-like metal targets using wideband electromagnetic induction," *IEEE Trans. Geoscience and Remote Sensing*, vol. 38. no. 3., pp. 1352–1361, 2000.
11. T. H. Bell, B. J. Barrow, and J. T. Miller, "Subsurface discrimination using electromagnetic induction sensors", *IEEE Transactions on Geoscience and Remote Sensing*, vol. 39 , no. 6, pp. 1286 – 1293, June 2001.
12. L. Carin, Yu Haitao; Y. Dalichaouch, A.R. Perry, P.V. Czipott, and C.E. Baum, "On the wideband EMI response of a rotationally symmetric permeable and conducting target," *IEEE Trans. Geoscience and Remote Sensing*, Vol. 39, No. 6, pp. 1206–1213, 2001.
13. J.T. Miller, T. Bell, J. Soukup, and D. Keiswetter, "Simple phenomenological models for wideband frequency-domain electromagnetic induction," *IEEE Trans. Geoscience and Remote Sensing.*, Vol. 39. No. 6., pp. 1294–1298, June 2001.

14. Y. Zhang, L. Collins, H. Yu, C. Baum, and L. Carin, "Sensing of unexploded ordnance with magnetometer and induction: theory and signal processing," *IEEE Trans. Geoscience and Remote Sensing,* Vol. 41, No. 5, pp. 1005–1015, May 2003.
15. X. Chen, K. O'Neill, B. E. Barrowes, T. M. Grzegorczyk, and J. A. Kong, "Application of a spheroidal-mode approach and a differential evolution algorithm for inversion of magneto-quasistatic data in UXO discrimination," *Inv. Prob.*, vol. 20, no. 6, pp. S27–S40, Dec. 2004.
16. F. Shubitidze, K. O'Neill, B. Barrowes, J. P. Fernández, I. Shamatava, K. Sun, and K. D. Paulsen, "Application of the normalized surface magnetic charge model to UXO discrimination in cases with overlapping signals", *Journal of Applied Geophysics*, vol. 61, pp. 292–303, 2007.
17. F. Shubitidze, O'Neill, K., I. Shamatava, K. Sun, and K.D. Paulsen, "Analysis of EMI scattering to support UXO discrimination: Heterogeneous and multi objects," In *Proc. of SPIE "Detection and Remediation Technologies for Mines and Mine Like Targets*," Orlando, Florida USA, pp. 928–939, April 21–25, 2003.
18. K. Sun, K. O'Neill, F. Shubitidze, I. Shamatava, and K. D. Paulsen, "Fast data-derived fundamental spheroidal excitation models with application to UXO discrimination," *IEEE Trans. Geosci. Remote Sens.*, vol. 43, no. 11, pp. 2573–2583, Nov. 2005.
19. F. Shubitidze, K. O'Neill, I. Shamatava, K. Sun, and K. D. Paulsen, "A fast and accurate representation of physically complete EMI response by a heterogeneous object," *IEEE Trans. Geosci. Remote Sens.*, vol. 43, no. 8, pp. 1736–1750, Aug. 2005.
20. F. Shubitidze, B. E. Barrowes, I. Shamatava, J. P. Fernández, and K. O'Neill, "Data derived generalized SEA applied to MPV TD data", Submitted, *The 24th International Review of Progress in Applied Computational Electromagnetics (ACES 2008)* March 30 – April 4, 2008, Niagara Falls, Canada.
21. F. Shubitidze, I. Shamatava, A. Bijamov, E. Demidenko "Combining dipole and mixed models approaches for UXO discrimination", *SPIE-2008*, Orlando Florida, March 16-21, 2008.
22. Steven A. Arcone, "Ground-Penetrating Radar Survey of Sub-bottom Munitions in a Small New England Lake", *in* Proceedings Partners in Environmental Technology Technical Symposium & Workshop, Washington DC, November 2006.
23. Jim McDonald, "UXO Detection and Characterization in the Marine Environment" *in p*roceedings Partners in Environmental Technology Technical Symposium & Workshop, Washington DC, November 2006.
24. Norton, S.J.; SanFilipo, W.A.; Won, I.J.; "Eddy-current and current-channeling response to spheroidal anomalies**".** GeoScience and Remote Sensing, IEEE Trans. vol. 43, Issue 10, Oct. 2005 pp:2200 – 2209.
25. Stalnaker, J.L.; Everett, M.E.; Benavides, A.; Pierce, C.J., Jr.; **"**Mutual induction and the effect of host conductivity on the EM induction response of buried plate targets using 3-D finite-element analysis Geoscience and Remote Sensing, IEEE Transactions on Volume 44, Issue 2, Feb. 2006 Page(s):251 – 259.
26. F. Shubitidze, K. O'Neill, S.A. Haider, K. Sun, and K.D. Paulsen,"Application of the method of auxiliary sources to the wideband electromagnetic induction problem," IEEE Trans. Geoscience and Remote Sensing, 40(4), 928–942, April 2002.
27. Shamatava, I., Shubitidze, F., O'Neill, K., Sun, K., and Paulsen, K.D. (2004). "An Efficient, User-Friendly Program for Computing Electromagnetic Induction (EMI) Responses from Heterogeneous Objects Subject to State-Of-The-Art Sensors," Proceedings of the UXO/Countermine Forum 2004, St. Louis, Missouri, 8-12 Mar 2004.
28. Shubitidze F., O'Neill K., Sun K., Shamatava I., and Paulsen K., 2004, A hybrid full MAS and combined MAS/TSA algorithm for electromagnetic induction sensing, Journal of applied computational electromagnetic society, 19 b, pp. 112-125.
29. Shubitidze F., O'Neill K., Shamatava I., Sun K., and Paulsen K, 2004, A fast and accurate representation of physically complete EMI response by a heterogeneous object, IEEE Trans. Geosci. & remote sensing, Volume 8, pp 1151-1162.
30. Keli Sun; O'Neill, K.; Shubitidze, F.; Haider, S.A.; Paulsen, K.D., "Theoretical analysis of TSA formulation and its domain of validity," *Geoscience and Remote Sensing, IEEE Transactions on* Volume 42, Issue 9, pp. 1871–1881, Sept. 2004.